Inorg. Chem. **2008**, *47*, 2649−2660

Probing Variable Amine/Amide Ligation in $Ni^{II}N_2S_2$ Complexes Using Sulfur K-Edge and Nickel L-Edge X-ray Absorption Spectroscopies: Implications for the Active Site of Nickel Superoxide Dismutase

Jason Shearer,* **Ahmad Dehestani**,† **and Franklin Abanda**

Department of Chemistry, University of Nevada, Reno, Nevada 89557

Received October 8, 2007

Nickel superoxide dismutase (NiSOD) is a recently discovered metalloenzyme that catalyzes the disproportionation of $O_2^{\bullet-}$ into O_2 and H_2O_2. In its reduced state, the mononuclear Ni^{II} ion is ligated by two *cis*-cysteinate sulfurs, an amine nitrogen (from the protein N-terminus), and an amide nitrogen (from the peptide backbone). Unlike many small molecule and metallopeptide-based NiN_2S_2 complexes, S-based oxygenation is not observed in NiSOD. Herein we explore the spectroscopic properties of a series of three $Ni^{II}N_2S_2$ complexes (bisamine-ligated (bmmp-dmed)Ni^{II}, amine/amide-ligated $(Ni^{II}(BEAAM))^-$, and bisamide-ligated $(Ni^{II}(emi))^{2-}$) with varying amine/amide ligation to determine the origin of the dioxygen stability of NiSOD. Ni L-edge X-ray absorption spectroscopy (XAS) demonstrates that there is a progression in ligand-field strength with (bmmp-dmed)Ni^{II} having the weakest ligand field and $(Ni^{II}(emi))^{2-}$) having the strongest ligand field. Furthermore, these Ni L-edge XAS studies also show that all three complexes are highly covalent with $(Ni^{II}(BEEAM))^-$ having the highest degree of metal–ligand covalency of the three compounds studied. S K-edge XAS also shows a high degree of Ni−S covalency in all three complexes. The electronic structures of the three complexes were probed using both hybrid-DFT and multiconfigurational SORCI calculations. These calculations demonstrate that the nucleophilic Ni(3d)/S(π)* HOMO of these NiN_2S_2 complexes progressively decreases in energy as the amide-nitrogens are replaced with amine nitrogens. This decrease in energy of the HOMO deactivates the Ni-center toward O_2 reactivity. Thus, the Ni−S bond is protected from S-based oxygenation explaining the enhanced stability of the NiSOD active-site toward oxygenation by dioxygen.

Nickel superoxide dismutases (NiSODs) are recently discovered metalloenzymes that catalyzes the disproportionation of superoxide ($O_2^{\bullet-}$) into dioxygen and hydrogen peroxide by cycling between reduced Ni^{II} and oxidized Ni^{III} oxidation states (Scheme 1).[1] X-ray crystallography revealed that NiSOD contains a mononuclear *cis*-cysteinate-ligated Ni center (from Cys^2 and Cys^6).[2] In the reduced Ni^{II} oxidation state, the Ni center is contained in a square-planar coordination geometry and is ligated by two additional nitrogen-based ligands from the N-terminal amine and an amide nitrogen (of Cys^2) derived from the peptide backbone. Upon oxidation to Ni^{III}, an additional nitrogen from the His^1 imidazole coordinates to the Ni-center forming a square pyramid.

Scheme 1

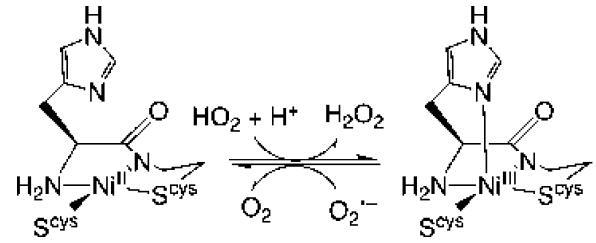

The Ni coordination environment observed in NiSOD is rather unusual, especially in the context of an SOD. First, transition metal–thiolates are highly susceptible to sulfur-

* To whom correspondence should be addressed. E-mail: shearer@unr.edu.
† Current address: Los Alamos National Laboratories, Los Alamos, NM.

(1) (a) Youn, H. D.; Kim, E. J.; Roe, J. H.; Hah, Y. C.; Kang, S. O. *Biochem. J.* **1996**, *318*, 889–896. (b) Youn, H. D.; Youn, H.; Lee, J. W.; Yim, Y. I.; Lee, J. K.; Hah, Y. C.; Kang, S. O. **1996**, *334*, 341–348. (c) Palenik, B.; Brahamsha, B.; Larimer, F. W.; Land, M.; Hauser, L.; Chain, P.; Lamerdin, J.; Regala, W.; Allen, E. E.; McCarren, J.; Paulsen, I.; Dufresne, A.; Partensky, F.; Webb, E. A.; Waterbury, J. *Nature* **2003**, *424*, 1037–1042.
(2) (a) Wuerges, J.; Lee, J. W.; Yim, Y. I.; Yim, H. S.; Kang, S. O.; Carugo, K. D. *Proc. Natl. Acad. Sci. U.S.A.* **2004**, *101*, 8569–8574. (b) Barondeau, D. P.; Kassmann, C. J.; Bruns, C. K.; Tainer, J. A.; Getzoff, E. D. *Biochemistry* **2004**, *43*, 8038–8047.

10.1021/ic7019878 CCC: $40.75
Published on Web 03/11/2008

based oxidation by O_2 and H_2O_2.[3] The NiSOD active site is exposed to both of these oxidants, yet the active site does not undergo sulfur-based oxidation. Two other unusual aspects of the NiSOD active site involves two of its nitrogen-based ligands. The amide−metal coordination motif is only found in a handful of metalloproteins,[4] while the use of the N-terminal amine as a ligand to a metal center is only found in one other metalloprotein, the CO sensor protein CooA.[5] Altogether, these observations suggest two important questions: *why does NiSOD utilize these unusual N-based ligands, and how do the sulfur-based ligands avoid oxidative damage?*

A number of recent studies have been aimed at addressing the influence that the NiSOD coordination environment has on the Ni centers' reactivity, stability, and physical properties.[6–9] Spectroscopic and computational studies by Brunold and co-workers[8] have demonstrated that the NiSOD active site is highly covalent in both the reduced and oxidized states; there is a large degree of S and Ni character found in the redox-active molecular orbital (RAMO) for both the Ni^{II} and Ni^{III} forms of the metalloenzyme. Furthermore, those studies have suggested that an increase in the number of amide-based nitrogen ligands to the metal-center will decrease the degree of sulfur character in favor of Ni character in the RAMO.[8a] This, it was suggested, was the key to providing the active-site protection from sulfur-based oxidative damage upon oxidation by $O_2^{\bullet-}$; the higher degree of Ni character ensures a metal-based, as opposed to sulfur-based, redox process.

Another study by Grapperhaus and co-workers has also focused on the stability of the NiSOD active site as a function of the nitrogen-based ligands.[9a] In that computational study the influence of variable N-ligation to several $Ni^{II}N_2S_2$ complexes was probed. Similar to Brunold's study, it was determined that as the number of amine ligands are exchanged for amide ligands the degree of S-character decreased in the RAMO. However, they suggested that protection from oxidative damage to the thiolate ligands was provided by a decrease in the energy of the HOMO upon going from amides to amines. This change in energy deactivates the Ni−S(π)* HOMO toward reactivity with O_2 and H_2O_2, thus providing the sulfurs protection from oxidation.

In this study, we will expand upon our previous work with the synthetic NiSOD analogue $(Ni^{II}(BEAAM))^-$ (Chart 1).[6c]

Chart 1

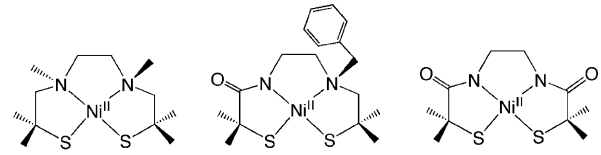

This complex contains Ni^{II} in a mixed N_2S_2 ligand environment with amide- and amine-based nitrogen ligands. Herein we will probe the electronic structure of $(Ni^{II}(BEAAM))^-$ using S K-edge and Ni L-edge X-ray absorption spectroscopy (XAS), electronic absorption spectroscopy, and electronic structure calculations. The structurally related bis-amine ligated (bmmp-dmed)Ni^{II} and bis-amide ligated $(Ni(emi))^-$ (Chart 1)[10] will also be probed by the above methods. Thus, we will be able to explore in detail how a systematic change in the nitrogen ligands from amines to amides is influencing the electronic structure of $Ni^{II}N_2S_2$ complexes. This study will therefore shed further light onto the role of the mixed amine/amide coordination environment in NiSOD.

Experimental Section

S K-edge X-ray Absorption Spectroscopy. Sample Preparation and Data Collection. Under an atmosphere of dinitrogen, the nickel complexes $[Et_4N]_2(Ni^{II}(emi))$,[10b] $[Me_4N](Ni^{II}(BEAAM))$,[6c] and (bmmp-dmed)Ni^{II}[10a] were finely ground. MeCN solutions of air-exposed $[Et_4N]_2$-$(Ni^{II}(emi))$ were evaporated to dryness, and the resulting brown powders were finely ground. The powders were then placed onto sulfur-free Kapton tape (verified by scanning the tape over the energy range used in this study) forming thin layers. These were then mounted onto polycarbonate sample holders. Data were then collected at room temperature on beamline X19A at the National Synchrotron Light Source (Brookhaven National Laboratories; Upton, NY). Spectra were recorded in fluorescence mode using a passivated implanted planar silicon detector (Canberra Industries). The X-ray beam passed from an incident ionization chamber to the sample chamber, which were both continually purged with He and separated from one another by polyethylene windows (5 μm thickness). Data were collected from 200 eV below the edge to 300 eV above the edge. In the pre-edge region (2270−2465 eV) data were collected in 5 eV steps; in the edge region (2465−2475 eV) data were collected in 0.1 eV steps, and in the near-edge region (2475−2765 eV) data were collected in 0.5 eV steps. All spectra were calibrated against the spectrum of elemental sulfur (first inflection point 2496.1 eV),[11] which was recorded in between each scan. The energy was found to drift by less than 0.1 eV from scan to scan. All reported spectra represent the average of 4 scans.

Data Analysis. Data were averaged and a baseline was applied to each spectrum by fitting the pre-edge region to a

(3) Grapperhaus, C. A.; Darensbourg, M. Y. *Acc. Chem. Res.* **1998**, *31*, 451–459.
(4) Kovacs, J. A. *Chem. Rev.* **2005**, *104*, 825–848.
(5) Lanzilotta, W. N.; Schuller, D. J.; Thorsteinsson, M. V.; Kerby, R. L.; Roberts, G. P.; Poulos, T. L. *Nat. Struct. Biol.* **2000**, *7*, 876–880.
(6) (a) Shearer, J.; Long, L. M. *Inorg. Chem.* **2006**, *45*, 2358–2360. (b) Neupane, K. P.; Shearer, J. *Inorg. Chem.* **2006**, *45*, 10552–10566. (c) Shearer, J.; Zhao, N. *Inorg. Chem.* **2006**, *45*, 9637–9639.
(7) (a) Pelmenschikov, V.; Siegbahn, P. E. M. *J. Am. Chem. Soc.* **2006**, *128*, 7466–7475. (b) Rajeev, P.; Keiji, M.; Djamaladdin, M. *J. Comput. Chem.* **2006**, *27*, 1438–1445.
(8) (a) Fiedler, A. T.; Bryngelson, P. A.; Maroney, M. J.; Brunold, T. C. *J. Am. Chem. Soc.* **2005**, *127*, 5449–5462. (b) Fiedler, A. T.; Brunold, T. C. *Inorg. Chem.* **2007**, *46*, 8511–8523.
(9) (a) Mullins, C. S.; Grapperhaus, C. A.; Kozlowski, P. M. *J. Biol. Inorg. Chem.* **2006**, *11*, 617–625. (b) Green, K. N.; Brothers, S. M.; Jenkins, R. M.; Carson, C. E.; Grapperhaus, C. A.; Darensbourg, M. Y. *Inorg. Chem.* **2007**, *46*, 7536–7544.
(10) (a) Grapperhaus, C. A.; Mullins, C. S.; Kozlowski, P. M.; Mashuta, M. S. *Inorg. Chem.* **2004**, *43*, 2859–2866. (b) Krüger, H.-J.; Peng, G.; Holm, R. H. *Inorg. Chem.* **1991**, *30*, 734–742.
(11) George, G. N.; Gorbaty, M. L. *J. Am. Chem. Soc.* **1989**, *111*, 3182–3186.

polynomial function. This baseline was then subtracted from the whole spectrum. The region above the edge jump was then fit to a two knot cubic spline, and the data normalized to the edge height. Pre-edge and the rising-edge features were modeled as pseudo-Voigt line shapes (a 1:1 sum of Gaussian and Lorentzian line shapes). Each spectrum required the use of only one peak per feature, and valid fits to the data were judged by matches to the second derivatives of the spectra. The intensity values of the pre-edge features, which represent the average of four different fits to the data (differing by less than 2%), are the products of the peak widths at half-height and intensities of the pseudo-Voigt line shapes. All pre-edge intensities were then converted into $\%S_{3p}$ character using the pre-edge feature of Ni(DACO) as a standard (46(2)%),[12] which by our fitting procedure corresponds to an intensity of 1.22(1) units.

Ni L-edge X-ray Absorption Spectroscopy. Sample Preparation and Data Collection. Ni L-edge X-ray absorption spectra were collected at the National Synchrotron Light Source, Brookhaven National Laboratories (Upton, NY), on beamline U4b.[13] Samples were prepared by application of finely ground powders of $[Et_4N]_2(Ni^{II}(emi))$, $[Me_4N](Ni^{II}$-(BEAAM)), or (bmmp-dmed)Ni^{II} to double-sided carbon tape (SPI Supplies). Spectra were recorded in total electron yield mode at ambient temperature under a vacuum of less than 5×10^{-8} mbar. The incident flux was measured from the total electron yield of a gold-coated grid placed between the monochromator and focusing mirror. Data were recorded in 0.4 eV steps prior to the L_3-edge (830−850 eV), 0.1 eV steps between the L_3 and L_2 edges (850−876 eV), and 0.4 eV steps beyond the L_2-edge (876−980 eV). Each spectrum reported represents the average of at least 3 data sets. Individual data sets were calibrated against a simultaneously recorded spectrum of nickel oxide (absorption maximum at 853.2 eV) and were inspected to ensure that sample decomposition was not occurring.

Data Analysis. The L-edge data analysis first involved the subtraction of the baseline obtained from the spectrum of a blank sample and then normalization of the spectra to 1.00 at an energy of 950 eV.[14] The L_3 (850−858 eV) and L_2 (865−876 eV) integrated intensities were then obtained by integration of the area under the respective peaks. For a standard we used Ni(DACO), which has ∼24% Ni3d character per hole (for a total of 48% Ni3d character in the LUMO).[12,15] For the spectral analysis, the background was removed from each spectrum by first fitting the region before the L_3- and after the L_2-edge to a polynomial function, followed by the removal of the intrinsic background caused by promotion of the 2p electrons to the vacuum as previously reported.[6b] The spectra were modeled using the TT-Multiplets suite of programs.[16] All of the spectra were modeled by calculating the atomic Ni^{II} spectra and extending the atomic Hamiltonian to include perturbations for both crystal-field and charge-transfer effects.[16b,17] Ni^{II} was simulated using D_{4h} symmetry (yielding energies for $10D_q$, D_t, and D_s). Furthermore, transitions from two different configurations were examined: $|Ni2p^63d^8\rangle \rightarrow |Ni2p^53d^9\rangle$ and $|Ni2p^63d^9\underline{L}\rangle \rightarrow |Ni2p^53d^{10}\underline{L}\rangle$, where $\underline{L}$ represents a hole in a previously filled ligand orbital. Simulations of the charge transfer states yields the energy difference of the two ground states (Δ), the two excited states (Δ_f), and the transfer integrals for the four sets of d-orbitals under D_{4h} symmetry (T_{A1g}, T_{B1g}, T_{B2g}, and T_{Eg}). Simulations of the spectra were produced by application of a Lorentzian line shape, followed by a Gaussian line shape to each transition (to approximate broadening caused by lifetime effects and the beamline optics), within the TT-Multiplets computer package.

Electronic Absorption Spectroscopy. All electronic absorption spectra were recorded at room temperature as MeCN solutions. Spectra were obtained on an OLIS-CARY 14 in quartz cuvettes with 1 cm pathlengths. The spectra were simulated as sums of Gaussian line shapes using the minimum number of peaks (three or four over the range of 11 000−25 000 cm^{-1}) to adequately simulate the spectrum as judged by matches to the second derivatives of the spectrum. The resulting fits are based on the average of three different spectral simulations, which varied by no more than 1% from each other.

Electronic Structure Calculations. Geometry optimizations (GOs) were performed using the Amsterdam Density Functional (ADF) software package version 2005.01.[18] The frozen core approximation was used for the 1s orbital of all second row elements and the 1s, 2s, and 2p orbitals for Ni and S. The valance orbitals were treated with the ADF TZDP (triple-ζ with double polarization) basis set. Calculations were performed using the local density approximation of Vosko, Wilk, and Nussair and the nonlocal gradient corrections of Beck and Perdew.[19]Single-point and frequency calculations[20a] were performed on these GO structures using Neese's electronic structure software package ORCA 2.6.4.[20b] All calculations were spin-restricted and used Ahlrichs' triple-ζ

(12) Dey, A.; Jeffrey, S. P.; Darensbourg, M. Y.; Hodgson, K. O.; Hedman, B.; Solomon, E. I. *Inorg. Chem.* **2007**, *46*, 4989–4996.
(13) Chen, C. T.; Sette, F. *Rev. Sci. Instrum.* **1989**, *60*, 1616–1621.
(14) Wang, H.; Ge, P.; Riordan, C. G.; Brooker, S.; Woomer, C. G.; Collins, T.; Melendres, C. A.; Graudejus, O.; Bartlett, N.; Cramer, S. P. *J. Chem. Phys. B* **1998**, *102*, 8343–8346.
(15) There is an uncertainty of at least ±2% Ni character in the LUMO of Ni(DACO).
(16) (a) Cowan, T. *The Theory of Atomic Structure and Spectra*; University of California Press: Berkeley, CA, 1981. (b) deGroot, F. M. F. *Chem. Rev.* **2001**, *101*, 1779–1808. (c) deGroot, F. M. F. *J. Electron Spectrosc. Relat. Phenom.* **1994**, *67*, 529–622.
(17) (a) Butler, P. H. *Point Group Symmetry: Applications, Methods, and Tables*; Plenum Press: New York, 1981. (b) Okada, K.; Kotani, A.; Thole, B. T. *J. Electron Spectrosc. Relat. Phenom.* **1992**, *58*, 325–343.
(18) Te Velde, G.; Bickelhaupt, F. M.; Baerends, E. J.; Guerra, C. F.; Van Gisbergen, S. J. A.; Snijders, J. G.; Ziegler, T. *J. Comput. Chem.* **2001**, *22*, 931–967.
(19) (a) Vosko, S. J.; Wilk, M.; Nussair, M. *Can. J. Phys.* **1980**, *58*, 1200–1211. (b) Becke, A. *J. Chem. Phys.* **1986**, *84*, 4524–4529. (c) Becke, A. *J. Chem. Phys.* **1988**, *88*, 1053–1062. (d) Becke, A. *Phys. Rev. A* **1988**, *38*, 3098–3100. (e) Perdew, J. P. *Phys. Rev. B* **1986**, *34*, 7406. (f) Perdew, J. P. *Phys. Rev. B* **1986**, *33*, 8822–8824.
(20) (a) Fan, L.; Ziegler, T. *J. Chem. Phys.* **1992**, *96*, 9005–9012. (b) Neese, F. *ORCA, An Ab Initio, Density Functional, and Semiempirical Program Package*, version 2.6.0; Institute for Physical and Theoretical Chemistry, Universität Bonn: Bonn, Germany; 2006.
(21) (a) Schaefer, A.; Horn, H.; Ahlrichs, R. *J. Chem. Phys.* **1992**, *97*, 2571. (b) Ahlrichs, R. and coworkers. Unpublished results.

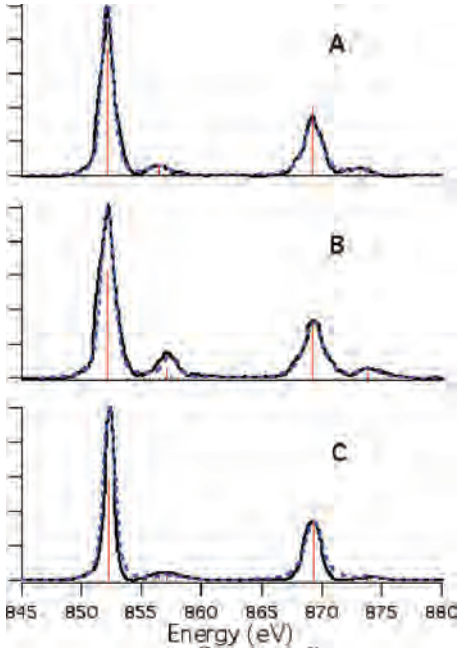

Figure 1. Ni L-edge XAS of (bmmp-dmed)Ni^{II} (**A**), (Ni^{II}(BEAAM))$^-$ (**B**), and (Ni^{II}(emi))$^{2-}$ (**C**). The data are presented as black solid lines; the simulations to the data are presented as dashed blue lines, and the individual transitions are presented as the vertical red sticks.

valence basis set with two sets of first polarization functions on all atoms (TZVPP).[21a,b] These calculations used Becke's three-parameter hybrid functional for exchange along with the Lee–Yang–Parr correlation functional.[22] The frequency calculations used two-sided displacements with a convergence accuracy of 10^{-7} E_h in total energy, 10^{-6} in density, and a Lebedev angular mesh of 434 points. Atomic orbital contributions to the resulting molecular orbitals are reported as Mulliken populations. Isosurface plots of the MOs were generated using the program gOpenMol 3.00.[23] Excitation energies were examined using the spectroscopy oriented configuration interaction (SORCI) formalism of Neese.[24] The CAS(8,5) reference space was employed. The selection threshold (T_{sel}) was set to 10^{-6} E_h; the prediagonalization threshold (T_{pre}) was set to 10^{-6}, and the natural orbital selection threshold (T_{nat}) was set to 10^{-5}.

Results

Nickel L-edge XAS. The Ni L-edge X-ray absorption spectra of (bmmp-dmed)Ni^{II}, (Ni^{II}(BEAAM))$^-$, and (Ni^{II}(emi))$^{2-}$ are displayed in Figure 1. As can be seen, the overall shape of the X-ray absorption spectra are similar to one another. The position of the main L_3 edges (~853.4 eV) and branching ratios ((bmmp-dmed)Ni^{II}, 0.69; (Ni^{II}(BEAAM))$^-$, 0.69; (Ni^{II}(emi))$^{2-}$, 0.66) are indicative of low-spin Ni^{II} centers.[25] All of the L-edge spectra display a relatively featureless main L_3 transition with satellite peaks ~5 eV higher in energy. These satellite peaks all display multiplet character. Similarly, the main L_2 transitions also have satellite peaks ~5 eV higher in energy. Such Ni L-edge spectra are typical of d^8 transition metal complexes with highly covalent ligand–metal bonds.[26]

Table 1. Ni L-Edge Results and Simulation Parameters for (bmmp-dmed)Ni^{II}, (Ni^{II}(BEAAM))$^-$, and (Ni^{II}(emi))$^{2-a}$

	(bmmp-dmed)Ni^{II}	(Ni^{II}(BEAAM))$^-$	(Ni^{II}(emi))$^{2-}$
L_3-edge maxima	853.3	853.4	853.4
L_2-edge maxima	870.4	870.5	870.2
Ni character in the LUMO (total)	60(6)%	57(6)%	68(7)%
$10D_q$	2.50	2.60	2.80
D_s	0.15	0.20	0.15
D_t	0.45	0.40	0.45
Δ	0.4	0.8	0.7
Δ_f	−1.6	−2.3	−1.3
T_{B1g}	1.90	2.25	2.10
T_{Eg}	2.10	1.85	0.10
T_{B2g}	0.35	0.25	0.10
T_{A1g}	0.10	0.10	0.10
$\|3d^8\rangle^b$	66%	63%	71%

[a] All values are given in eV except where noted. [b] Percent $Ni3d^8$ character in the ground-state wave function.

Because of the localized nature of the Ni2(p) orbital, the acceptor wave function must have Ni character for the L-edge transition to have any intensity.[27,28a,b] Thus, integration of the L_3 and L_2 edges of the Ni L-edge spectra will give a quantitative value for the Ni-ligand covalency of the three complexes investigated. The three Ni L-edge spectra were all normalized to an edge jump of 1.00 at 950 eV (Supporting Information). Ni(DACO), which has ~48% Ni character in its LUMO,[12,15] was used as a standard yielding an integrated intensity of 17.2 units. This corresponds to 2.8% Ni character in the LUMO per unit of intensity. Because of the errors associated with the uncertainty in the %Ni character in the LUMO of Ni(DACO) and the experimental errors inherent in the L-edge experiment, we estimate approximately a 10% uncertainty in this value. Integration of the L-edge spectra for the three complexes yields 60(6)% Ni character in the LUMO of bis-amine-ligated (bmmp-dmed-)Ni^{II}, 57(6)% Ni character in the LUMO of amine/amide ligated (Ni^{II}(BEAAM))$^-$, and 68(7)% Ni character in the LUMO of bis-amide-ligated (Ni(emi))$^{2-}$ (Table 1). This indicates that the Ni complexes investigated all have strong Ni-ligand bonding interactions.

To account for the Ni-ligand covalency in these systems, the L-edge simulations (using the TT-multiplets computer suite) invoked a valence bond configuration interaction

(22) (a) Becke, A. D. *J. Chem. Phys.* **1993**, *98*, 5648–5652, 1372–1377. (b) Lee, C. T.; Yang, W. T.; Parr, R. G. *Phys. Rev. B: Condens. Matter* **1988**, *37*, 785–789.
(23) (a) Bergman, D. L.; Laaksonen, L.; Laaksonen, A. *J. Mol. Graphics Modell.* **1997**, *15*, 301. (b) Laaksonen, L. *J. Mol. Graphics* **1992**, *10*, 33.
(24) Neese, F. *J. Chem. Phys.* **2003**, *119*, 9428–9443.
(25) Wang, H.; Ralston, C. Y.; Patil, D. S.; Jones, R. M.; Gu, W.; Verhagen, M.; Adams, M.; Ge, P.; Riordan, C.; Marganian, C. A.; Mascharak, P.; Kovacs, J.; Miller, C. G.; Collins, T. J.; Brooker, S.; Croucher, P. D.; Wang, K.; Stiefel, E. I.; Cramer, S. P. *J. Am. Chem. Soc.* **2000**, *122*, 10544–10552.
(26) van Elp, J.; Peng, G.; Searle, B. G.; Mitra-Kirtley, S.; Huang, Y.-H.; Johnson, M. K.; Zhou, Z. H.; Adams, M. W. W.; Maroney, M. J.; Cramer, S. P. *J. Am. Chem. Soc.* **1994**, *116*, 1918–1923.
(27) George, S. J.; Lowery, M. D.; Solomon, E. I.; Cramer, S. P. *J. Am. Chem. Soc.* **1993**, *115*, 2968–2969.

Scheme 2

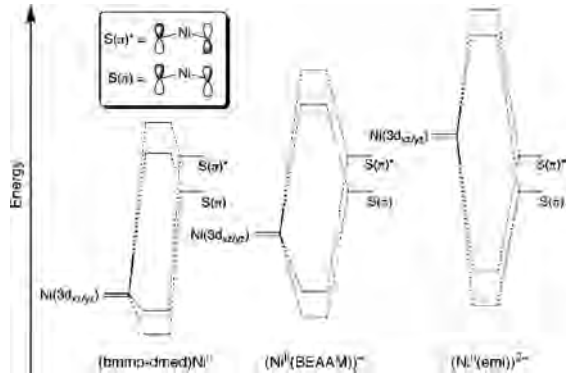

(VBCI) model.[28] Applied to these Ni^{II} complexes, the ground-state wave function can be represented as a linear combination of two different states: the $|Ni2p^63d^8\rangle$ state and the $|Ni2p^63d^9\underline{L}\rangle$ charge transfer state (where $\underline{L}$ represents a ligand-based hole). The energy difference between the two states is represented by the energy Δ, while the two states are coupled together by a configuration interaction given by the transfer integral T ($T = \langle Ni2p^63d^8|H|Ni2p^63d^9\underline{L}\rangle$) (Scheme 2). Similarly, the L-edge final state can also be represented as a linear combination of two different excited configurations: $|Ni2p^53d^9\rangle$ and the $|Ni2p^53d^{10}\underline{L}\rangle$. These two configurations are separated by the energy Δ_f and are coupled by the final-state transfer integral T_f. The final-state parameter Δ_f is related to the ground-state term Δ by: $\Delta_f = \Delta + U - Q$ (where Q and U are the Ni 2p−3d (Q) and 3d−3d (U) electron correlation integrals). Therefore the excited-state term Δ_f is approximately 1−3 eV lower in energy than the ground-state term Δ. As is typically done in simulations of L-edge data within the VBCI model, the ground- and final-state terms T and T_f are assumed to be identical to one another for these L-edge simulations.

Simulations to the L-edge data were accomplished by first calculating the atomic spectrum for Ni^{II}, which employed a reduction in the relevant Slater–Condon integrals to 85% of their calculated atomic values to account for covalency.[26] This was followed by including a perturbation to the atomic Hamiltonian for crystal-field effects by lowering the symmetry of the Ni^{II} centers into D_{4h} symmetry. Doing so yielded the crystal-field parameters $10D_q$, D_s, and D_t. Additional perturbations were included to account for charge-transfer effects using the VBCI model (vide supra). Because these complexes are not spherically symmetric, there are different T (and T_f) values for each set of 3d orbitals reflecting differential orbital overlap between the metal and ligand orbitals.[26] Therefore, in addition to the parameters Δ and Δ_f, the transfer integrals T_{A1g}, T_{B1g}, T_{B2g}, and T_{Eg} are also obtained.

The parameters used in the simulation of the Ni L-edge spectra of (bmmp-dmed)Ni^{II}, $(Ni^{II}(BEAAM))^-$, and $(Ni^{II}(emi))^{2-}$ are listed in Table 1. As might be expected,[4,19] the three complexes all yielded similar crystal-field parameters, all of which are consistent with low-spin Ni^{II}.[29] $(Ni^{II}(emi))^{2-}$, where the Ni^{II} ion is ligated by a tetraanionic ligand, was modeled using the strongest crystal-field strength of the series ($10D_q = 2.80$ eV, $D_S = 0.15$ eV, $D_t = 0.45$ eV). In contrast (bmmp-dmed)Ni^{II}, where Ni^{II} ligated by a dianionic ligand, yielded the weakest crystal-field parameters ($10D_q = 2.50$ eV; $D_S = 0.15$ eV; $D_t = 0.45$ eV). $(Ni^{II}(BEAAM))^-$, where Ni^{II} is ligated by a trianionic ligand, displayed crystal-field parameters intermediate of $(Ni^{II}(emi))^{2-}$ and (bmmp-dmed)-Ni^{II} ($10D_q = 2.60$ eV, $D_S = 0.20$ eV, $D_t = 0.40$ eV). The resulting crystal-field splitting energy diagrams are displayed in Figure 2.

For all three Ni^{II} complexes investigated in this study, the Δ_f terms are negative. Thus, the $|Ni2p^53d^{10}\underline{L}\rangle$ configurations are all lower in energy than the $|Ni2p^53d^9\rangle$ configurations (i.e., inverted final states).[28b] Such a situation is consistent with the observed data. The main L_3 transitions are sharp featureless peaks. Because these peaks result from $|Ni2p^63d^9\underline{L}\rangle \rightarrow |Ni2p^53d^{10}\underline{L}\rangle$ transitions, they should lack multiplet structure. The higher-energy satellite peaks display fine structure. This is entirely consistent with a $|Ni2p^63d^8\rangle \rightarrow |Ni2p^53d^9\rangle$ transitions, which should display multiplet structure.

As was found with the integrated Ni L-edge intensities, the parameters obtained from the VBCI simulations for all three compounds are consistent with covalent Ni^{II} centers. From the VBIC simulations, we find that the ground-state wave functions are mostly $|Ni3d^8\rangle$ in character. $(Ni^{II}(BEAAM))^-$ was found to contain the lowest percentage of $|Ni3d^8\rangle$ character (63%) in its ground-state wave function, indicating it is the most-covalent Ni-center. This is followed by (bmmp-dmed)Ni^{II} ($|Ni3d^8\rangle = 66\%$) and then $(Ni^{II}(emi))^{2-}$ ($|Ni3d^8\rangle = 71\%$). These trends are consistent with the findings from the integrated Ni L-edge results; amine/amide-ligated $(Ni^{II}(BEAAM))^-$ was found to have the most-covalent LUMO and bis-amide ligated $(Ni^{II}(emi))^{2-}$ the least (vide supra).

The high degree of covalency in $(Ni^{II}(BEAAM))^-$ results mostly from a highly covalent b_{1g} orbital ($T_{B1g} = 2.25$ eV; this orbital results from ligand-based bonding interactions along the *xy* plane into the Ni($3d_{x^2-y^2}$) orbital). We note that the magnitude of the other transfer integrals also indicate a high degree of covalency in the other 3d orbitals of $(Ni^{II}(BEAAM))^-$ (Table 1). The decrease in the Ni-ligand covalency of (bmmp-dmed)Ni^{II} compared with that of $(Ni^{II}(BEAAM))^-$ is specifically the result of a reduction in the covalency of its b_{1g} orbital ($T_{B1g} = 1.90$ eV); the other transfer integrals are comparable to those observed for $(Ni^{II}(BEAAM))^-$. The reduction in the covalency of $(Ni^{II}(emi))^{2-}$ compared to that of $(Ni^{II}(BEAAM))^-$ is caused by a reduction in the magnitude of both T_{B1g} (2.10 eV) and the other three transfer integrals (Table 1).

Sulfur K-edge XAS. Ligand K-edge XAS has proven to be a powerful tool for probing the covalency of transition

(28) (a) Wasinger, E. C.; deGroot, F. M. F.; Hedman, B.; Hodgson, K. O.; Solomon, E. I. *J. Am. Chem. Soc.* **2003**, *125*, 12894–12906. (b) Sarangi, R.; Aboelella, N.; Fujisawa, K.; Tolman, W. B.; Hedman, B.; Hodgson, K. O.; Solomon, E. I. *J. Am. Chem. Soc.* **2006**, *128*, 8286–8296. (c) Kennepohl, P.; Solomon, E. I. *Inorg. Chem.* **2003**, *42*, 679–688. (d) Hu, Z.; Kaindl, G.; Müller, B. G. *Alloys Compd.* **1997**, *246*, 177–185. (e) Van der Laan, G.; Zaanen, J.; Sawatzky, G. A.; Karnatak, R.; Esteva, J. M. *Phys. Rev. B* **1986**, *33*, 4253–4263.

(29) Mixed amide/thiolate complexes are well known to produce low-spin complexes. See ref 4 and references therein.

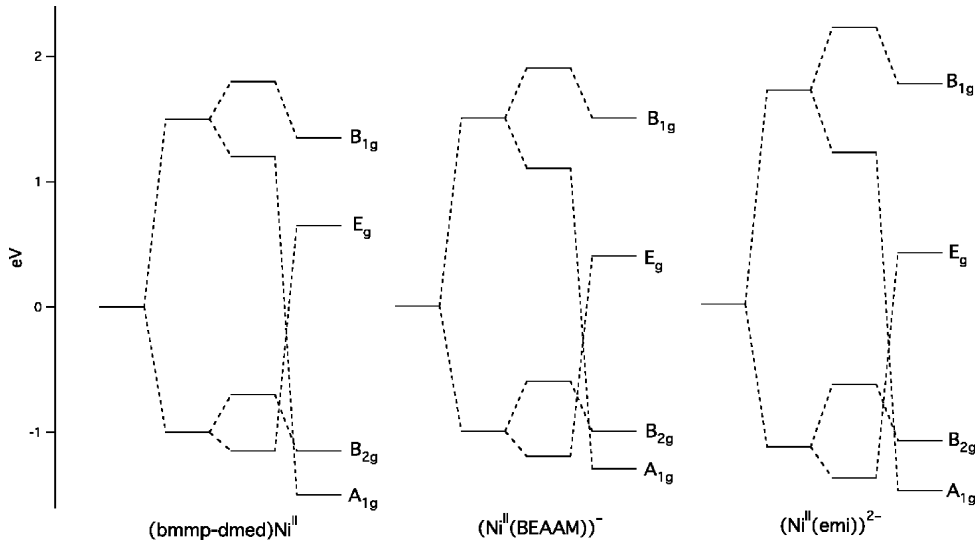

Figure 2. Ligand-field splitting diagrams derived from the L-edge simulation parameters of (bmmp-dmed)Ni^{II}, (Ni^{II}(BEAAM))$^-$, and (Ni^{II}(emi))$^{2-}$ upon lowering the symmetry from spherical symmetry to a O_h symmetry (application of $10D_q$) and to D_{4h} symmetry (application of D_s followed by D_t). The energy has been normalized to the degenerate d-orbitals in spherical symmetry.

metal complexes and has been used most extensively in the examination of thiolate-ligated transition metal complexes and metalloproteins.[30] In thiolate-ligated transition metal complexes containing one or more holes in the d-manifold the S K-edge is characterized by an intense low-energy pre-edge feature. This pre-edge feature corresponds to a S(1s) → M(d) transition. Because of the localized nature of the S(1s) orbital, the acceptor orbital wave function must contain S-character for this transition to have any intensity. The intensity of the pre-edge transition is given by

$$I(\mathrm{S(1s)} \rightarrow \mathrm{M(d)}) = \alpha^2 I(\mathrm{S(1s)} \rightarrow \mathrm{S(3p)}) \qquad (1)$$

where I(S(1s) → S(3p)) is the intensity of the purely ligand-based transition and α^2 is the ligand coefficient of the acceptor orbital wave function.[31] Thus, the intensity of the pre-edge feature in the S K-edge spectrum of a transition metal complex provides a direct measure of the metal–ligand covalency in the acceptor orbital (i.e., α^2).

The S K-edge XAS for (bmmp-dmed)Ni^{II}, (Ni^{II}(BEAAM))$^-$, and (Ni^{II}(emi))$^{2-}$ are displayed in Figure 3. All three spectra display a sharp pre-edge feature at ~2471 eV resulting from the S(1s) → LUMO transition. Upon going from (bmmp-dmed)Ni^{II} to (Ni^{II}(BEAAM))$^-$ to (Ni^{II}(emi))$^{2-}$, there is a progressive shift in energy of this pre-edge feature, consistent with the systematic destabilization of the LUMO (i.e., an increase in $10Dq$). Bis-amine-ligated (bmmp-dmed)Ni^{II} displays the lowest-energy S(1s) → LUMO transition (2470.7(1) eV), followed by amine/amide-ligated (Ni^{II}(BEAAM))$^-$ (2471.0(1) eV) and then by bis-amide-ligated (Ni^{II}(emi))$^{2-}$ (2471.4(1) eV). We note that the positions of the S(1s) → S(C−Sσ^*) transition (the rising-edge feature) is practically invariant in the metal complexes

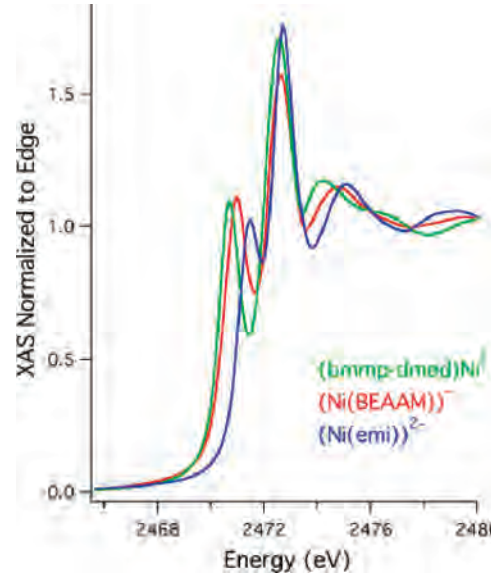

Figure 3. S K-edge X-ray absorption spectra of (bmmp-dmed)Ni^{II} (green), (Ni(BEAAM))$^-$ (red), and (Ni(emi))$^{2-}$ (blue).

Table 2. Sulfur K-Edge XAS Results for (bmmp-dmed)Ni^{II}, (Ni^{II}(BEAAM))$^-$, and (Ni^{II}(emi))$^{2-}$

	pre-edge position (eV)	rising-edge position (eV)	pre-edge intensity	covalency (%S_{3p}/hole)
(bmmp-dmed)Ni^{II}	2470.7(1)	2473.1(1)	0.92(1)	34(2)
(Ni^{II}(BEAAM))$^-$	2471.0(1)	2473.1(1)	0.93(1)	34(2)
(Ni^{II}(emi))$^{2-}$	2471.4(1)	2473.2(1)	0.74(1)	27(2)

examined (2473.1(1) eV for (bmmp-dmed)Ni^{II} and (Ni^{II}-(BEAAM))$^-$, and 2473.2(1) eV for (Ni(emi))$^{2-}$).

All of the observed S(3p) contributions to the LUMO are indicative of covalent Ni−S bonding, as was predicted by the simulations to the Ni L-edge spectra. The pre-edge intensities obtained from the fits to the data are displayed in Table 2. As an intensity standard the square-planar $Ni^{II}N_2S_2$ complex Ni(DACO) was used, which has an intensity of 1.22 units (by our fitting procedure) corresponding to the previously determined Ni−S covalency (%S(3p)/hole) of 46(2)%.[12] We find that the bis-amine-ligated (bmmp-

(30) (a) Glaser, Y.; Hedman, B.; Hodgson, K. O.; Solomon, E. I. *Acc. Chem. Res.* **2000**, *33*, 859–868. (b) Solomon, E. I.; Hedman, B.; Hodgson, K. O.; Dey, A.; Szilagyi, R. K. *Coord. Chem. Rev.* **2005**, *249*, 97–129.

(31) Neese, F.; Hedman, B.; Hodgson, K. O.; Solomon, E. I. *Inorg. Chem.* **1999**, *38*, 4854–4860.

dmed)Ni^{II} and amine/amide-ligated $(Ni(BEAAM))^-$ have essentially identical Ni−S covalencies in the LUMO acceptor orbital; both (bmmp-dmed)Ni^{II} and $(Ni^{II}(BEAAM))^-$ have 34(2)% S(3p) character in their acceptor orbitals. $(Ni^{II}(emi))^{2-}$ has the lowest degree of S(3p) character in its acceptor orbital (27(2)%) of the three complexes investigated.

The position of the rising-edge feature is caused by the effective charge on the sulfur and carbon atoms.[30] The approximate energy of this feature can be correlated to the oxidation state of the sulfur atom, and its position is consistent for M-thiolates in the case of all three Ni complexes studied. Fine changes in the position of the rising-edge feature can be correlated to difference in the Ni−S covalency. The less S character there is in the acceptor state wave function, the higher in energy the rising-edge should shift. This is the result of an increase in Z_{eff} on the sulfur atom, which will in turn increase in the energy of the S(C−Sσ*) orbital. As explained above, the energies of the rising-edge features are nearly identical for (bmmp-dmed)Ni^{II} and $(Ni^{II}(BEAAM))^-$ versus that of $(Ni^{II}(emi))^{2-}$ when the experimental uncertainties are taken into account. This is not entirely expected. For the magnitude in the change of covalency observed in these three compounds, one may expect that the energy of the rising-edge should change by ~0.3 eV, not the 0.1(1) eV that was observed.[30b]

Ground-State Electronic Structure Calculations. Computational models for (bmmp-dmed)Ni^{II}, $(Ni^{II}(BEAAM))^-$, and $(Ni^{II}(emi))^{2-}$ were derived from the crystallographic data of the three compounds.[6c,10] To minimize the computational effort in the calculation of $(Ni^{II}(BEAAM))^-$, especially for the excited-state calculation (vide infra), the phenyl amine was replaced with a methyl amine. Geometry optimizations were then undertaken using density functional theory methods (DFT) using the computational package ADF2005.1 (TZDP; VWN/BP; see Figure 4 and Table 3).

The geometry-optimized (GO) structures are all consistent with the nature of the ligands to Ni^{II}. The amide ligands display a significant trans influence resulting in a lengthening of the trans Ni^{II}−S bonds when compared to the Ni^{II}−S bonds trans to the amine ligands. In addition, we observe asymmetry in the coordination environment about Ni in (bmmp-dmed)Ni^{II}, as was observed in the solid-state structure of the metal complex.[10a] This results from the geometric strain about the N-amine ligands. For the amine to adopt a near tetrahedral geometry, it must "pull" back the other amine ligand as a result of the ethylene backbone linker. This results in a significant lengthening of one Ni−amine bond relative to the other. As such, the Ni−S ligand trans to the longer amine obtains a stronger (and hence shorter) bonding interaction with Ni. Such a pronounced asymmetry is not present in $(Ni^{II}(emi))^{2-}$ because the linear nature of the amide ligand allows for significantly less strain in the five -membered chelate ring containing the N-amide ligand to Ni^{II}.

We note that all three complexes have calculated bond lengths that are slightly longer than the crystallographic data (Table 3). Previous studies have suggested that this should not have a major impact on the calculated energies when compared to better geometrically optimized structures.[7a,32] We confirmed this by performing B3LYP calculations (TZVPP) calculations using the crystallographic coordinates of the three complexes. These calculations yielded orbital coefficients and relative energies comparable to the B3LYP calculations performed on the DFT GO structures (Tables 4 and 6 and Supporting Information Tables S1–S3).

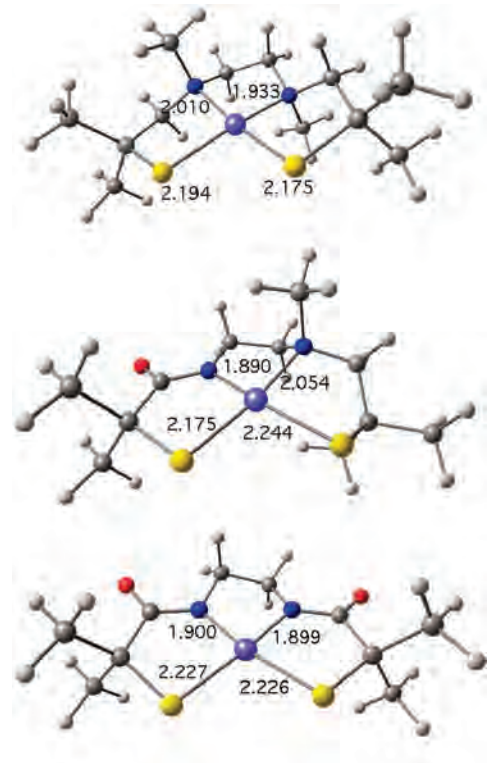

Figure 4. Geometry optimized structures of (bmmp-dmed)Ni^{II}, $(Ni^{II}(BEAAM))^-$, and $(Ni^{II}(emi))^{2-}$ with the Ni^{II}−ligand bond lengths (in Å) highlighted.

Table 3. Selected Computational (Top Values) versus Crystallographic (Bottom Values)[6c,10] Bond Lengths and Angles for (bmmp-dmed)Ni^{II}, $(Ni^{II}(BEAAM))^-$, and $(Ni^{II}(emi))^{2-}$

metrical parameter (Å or deg)	(bmmp-dmed)Ni^{II}[a]	$(Ni^{II}(BEAAM))^{-}$[a,b]	$(Ni^{II}(emi))^{2-}$[a]
Ni−S_1	2.175	2.244	2.227
	2.147(1)	2.177(2)	2.181(1)
Ni−S_2	2.194	2.175	2.226
	2.161(1)	2.137(2)	2.180(1)
Ni−N_1	2.010	1.890	1.900
	1.950(3)	1.858(6)	1.861(2)
Ni−N_2	1.933	2.054	1.899
	1.930(2)	1.989(7)	1.855(2)
N_1−Ni−N_2	89.03	86.43	85.82
	88.11(12)	85.8(3)	85.67(9)
S_1−Ni−S_2	96.00	97.28	99.13
	95.16(4)	97.52(8)	99.10(3)
N_1−Ni−S_1	169.82	169.11	172.83
	168.75(10)	168.9(2)	172.88(4)
N_1−Ni−S_2	88.41	90.34	87.56
	88.63(9)	90.0(2)	87.61(7)
N_2−Ni−S_1	89.85	88.47	87.61
	89.87(9)	88.3(2)	87.72(7)
N_2−Ni−S_2	167.13	168.93	172.97
	168.79(9)	168.9(2)	172.89(6)

[a] In these complexes S_1 is trans to N_1 and S_2 is trans to N_2. [b] For $(Ni^{II}(BEAAM))^-$, N_1 is the amide nitrogen and N_2 is the amine nitrogen.

(32) Siegbahn, P. E. M. *J. Comput. Chem.* **2001**, *22*, 1634–1645.

Table 4. Mulliken Population Analysis Based on the B3LYP Calculations for Selected Molecular Orbitals of (bmmp-dmed)Ni^{II}

MO label	MO	E (eV)	%Ni[a]	%N[b]	%S[c]	orbital composition[d]
LUMO	86	−1.11	53.2	4.7	38.9	$Ni(3d_{x^2-y^2}) - S(\sigma) - N(\sigma)$
HOMO	85	−4.40	18.3	<0.1	74.4	$S(\pi)^* - Ni(\pi)$
HOMO−1	84	−4.53	28.2	0.7	63.2	$S(\pi) - Ni(\pi)$
HOMO−2	83	−5.22	84.8	<0.1	14.0	$Ni(3d_{z^2}) - S(\sigma)$
HOMO−3	82	−5.96	38.1	6.0	47.7	$S(\sigma) + Ni - N(\sigma)$
HOMO−4	81	−6.30	30.7	6.5	53.4	$S(\pi) + Ni(3d_{xy})$
HOMO−5	80	−6.57	62.7	1.5	31.1	$Ni(3d_{xz}) + S(\pi)^* + N$
HOMO−6	79	−6.65	69.5	3.6	12.8	$Ni(3d_{xz}) + S(\pi) + N$

[a] AO contribution from the Ni 3d, 4s, and 4p orbitals. [b] AO contribution from the N 2s and 2p orbitals. [c] AO contribution from the S 3s, 3p, and 3d orbitals. [d] The composition is given in order of AO contribution to the AO. Bonding interactions are denoted with a + and antibonding interactions are denoted with a −.

Table 5. Mulliken Population Analysis Based on the B3LYP Calculations for Selected Molecular Orbitals of $(Ni^{II}(BEAAM))^-$

MO label	MO	E (eV)	%Ni[a]	%N[b]	%S[c]	orbital composition[d]
LUMO	85	2.53	52.9	9.9	37.8	$Ni(3d_{x^2-y^2}) - S(\sigma) - N(\sigma)$
HOMO	84	−1.14	32.7	0.3	50.3	$S(\pi)^* - Ni(\pi)$
HOMO−1	83	−1.37	39.1	4.1	37.2	$S(\pi) - Ni(\pi) - N/O(\pi)^*$[e]
HOMO−2	82	−1.79	86.4	<0.1	11.3	$Ni(3d_{z^2}) - S(\sigma)$
HOMO−3	81	−2.15	33.1	9.3	34.7	$S(\pi) + Ni - N/O(\pi)$[e]
HOMO−4	80	−2.42	11.9	13.8	35.1	$S(\pi) + Ni(3d_{xy}) - N/(\pi)$[f]
HOMO−5	79	−2.92	53.7	3.6	33.0	$Ni(3d_{xz}) + S(\pi)^* + N/O(\pi)$[e]
HOMO−6	78	−3.04	56.0	8.6	22.0	$Ni(3d_{xz}) + S(\pi) + N/O(\pi)$[e]

[a] AO contribution from the Ni 3d, 4s, and 4p orbitals. [b] AO contribution from the N 2s and 2p orbitals. [c] AO contribution from the S 3s, 3p, and 3d orbitals. [d] The major MO composition is given in order of AO contribution to the MO. Bonding interactions are denoted with a +, and antibonding interactions are denoted with a −. [e] There are minor contributions from the amide oxygen AOs (<2%) in these MOs. [f] The contribution from the O 2s and 2p orbitals in this MO is 26.5%.

Table 6. Mulliken Population Analysis Based on the B3LYP Calculations for Selected Molecular Orbitals of $(Ni^{II}(emi))^{2-}$

MO label	MO	E (eV)	%Ni[a]	%N[b]	%S[c]	%O[d]	orbital composition[e]
LUMO	84	6.24	56.0	12.6	29.6	1.4	$Ni(3d_{x^2-y^2}) - S(\sigma) - N(\sigma)$
HOMO	83	2.26	38.5	2.4	31.0	1.5	$Ni(\pi) - S(\pi)^*$
HOMO−1	82	2.08	43.7	7.4	36.6	5.9	$Ni(\pi) - S(\pi) - N/O(\pi)^*$
HOMO−2	81	1.74	96.6	0.2	3.0	0.5	$Ni(3d_{z^2}) - S(\sigma)$
HOMO−3	80	1.29	19.6	24.4	28.4	17.1	$S(\pi) + Ni - N/O(\pi)$
HOMO−4	79	1.07	16.2	7.9	46.6	20.7	$S(\pi) + Ni(3d_{xy}) - N/(\pi)$
HOMO−5	78	0.71	25.8	8.4	52.9	5.5	$S(\pi)^* + Ni(3d_{xz}) + N/O(\pi)$
HOMO−6	77	0.51	11.5	2.6	30.6	39.3	$S(\pi) + Ni(3d_{xz}) + N/O(\pi)$

[a] AO contribution from the Ni 3d, 4s, and 4p orbitals. [b] AO contribution from the N 2s and 2p orbitals. [c] AO contribution from the S 3s, 3p, and 3d orbitals. [d] AO contribution from the O 2s and 2p orbitals. [e] The major MO composition is given in order of AO contribution to the MO. Bonding interactions are denoted with a +, and antibonding interactions are denoted with a −.

The above DFT-derived GO structures were then used for single-point energy hybrid-DFT (B3LYP; TZVPP) calculations to gain a more detailed understanding of the electronic structure of these three Ni-complexes. As has been previously found by us and others,[6b,c,8a,10] the LUMO of $Ni^{II}N_2S_2$ complexes is composed of antibonding σ-interactions between the N and S p_z-orbitals and the $Ni(3d_{x^2-y^2})$ orbital. Consistent with our S K-edge data, the LUMO orbital progresses to higher energy relative to the essentially nonbonding $Ni(3d_{z^2})$ (the HOMO−2; Figure 5) as the N-amines are replaced with N-amides. We observe a calculated increase in the energy of the LUMO of 0.2 eV upon going from (bmmp-dmed)Ni^{II} to $(Ni^{II}(BEAAM))^-$ and a destabilization of an additional 0.2 eV upon going from $(Ni^{II}(BEAAM))^-$ to $(Ni^{II}(emi))^{2-}$.

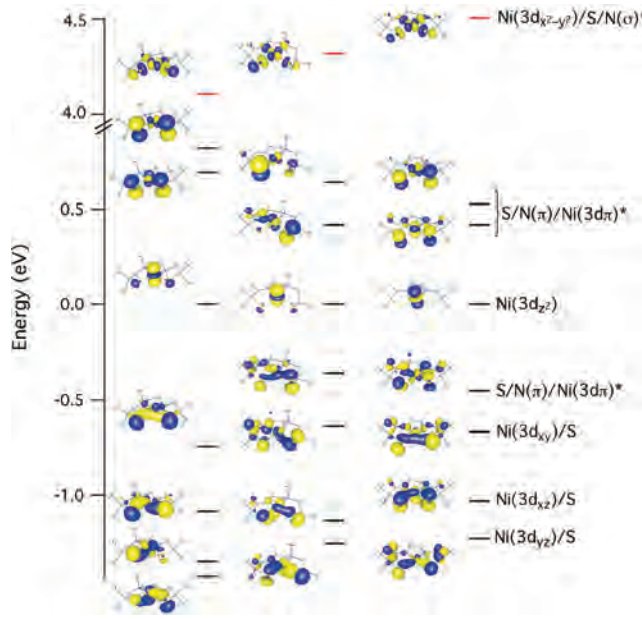

Figure 5. Molecular orbital energy level diagram and isosurface plots obtained from the B3LYP calculation of (bmmp-dmed)Ni^{II} (left), $(Ni^{I-I}(BEAAM))^-$ (middle), and $(Ni^{II}(emi))^{2-}$ (right). The isosurface plots correspond to the molecular orbital it is closest to. The molecular orbital labels on the right-hand side of the figure translate across the series. Filled orbitals are depicted as black lines, while unfilled orbitals are depicted as red lines.

Also consistent with the S K-edge data are the atomic orbital (AO) contributions to the LUMO. A Mulliken population analysis (Tables 4 and 6) reveals that the LUMO for (bmmp-dmed)Ni^{II} is composed of 37.1% S(p)-character; the LUMO for $(Ni(BEAAM))^-$ is composed of 35.6% S(p)-character, and the LUMO for $(Ni(emi))^{2-}$ is composed of 26.0% S(p)-character.[33] The reduction in S(p)-character as one goes from bis-amine ligated (bmmp-dmed)Ni^{II} to bis-amide ligated $(Ni^{II}(emi))^{2-}$ corresponds to a progressive increase in N-character (increasing from 4.7 to 12.6%). This is consistent with the structural data for these three complexes, where a significant trans amide effect was noted, which results from the stronger N-amide σ-bonding interactions compared to the N-amine ligands.

Electronic Absorption Spectroscopy and Excited-State Calculations. Figure 6 displays the electronic absorption spectra of (bmmp-dmed)Ni^{II}, $(Ni(BEAAM))^-$, and $(Ni(emi))^{2-}$ highlighting the ligand-field transitions (Table 7). All three spectra are qualitatively similar in this region, with a sharp higher-energy feature and broad lower intensity shoulder occurring at lower energies. However, there is a progressive shift to higher energies of these features as the amine-nitrogens are systematically replaced by amide-nitrogens. The prominent higher energy feature occurs at 20 900 cm^{-1} for (bmmp-dmed)Ni^{II}, 21 760 cm^{-1} for $(Ni^{II}(BEAAM))^-$, and 22 930 cm^{-1} for $(Ni^{II}(emi))^{2-}$, while the shoulders occur at 15 550 cm^{-1} for (bmmp-dmed)Ni^{II}, 17 070 cm^{-1} for $(Ni^{II}(BEAAM))^-$, and 18 120 cm^{-1} for $(Ni^{II}(emi))^{2-}$. To identify the transitions that comprise these

(33) The differences between the experimental %S character and computationally derived orbital coefficients could be caused by deviations in computational structures of the three complexes.

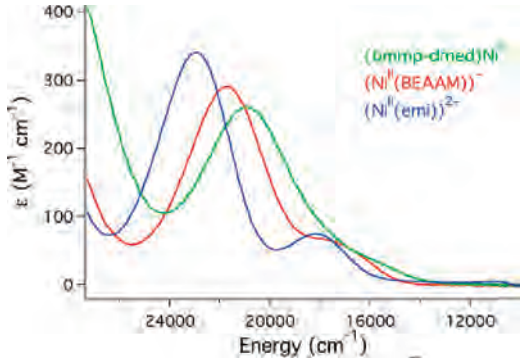

Figure 6. Electronic absorption spectra of (bmmp-dmed)Ni^{II} (green), $(Ni^{II}(BEAAM))^-$ (red), and $(Ni^{II}(emi))^{2-}$ (blue) highlighting the ligand-field region of the spectra.

Table 7. Experimentally Determined Spectral Parameters for (bmmp-dmed)Ni^{II}, $(Ni^{II}(BEAAM))^-$, and $(Ni^{II}(emi))^{2-}$[a]

band	energy (cm^{-1})	ϵ (M^{-1} cm^{-1})	f ($\times 10^{-3}$)[b]
(bmmp-dmed)Ni^{II}			
1	16 300	34	0.29
2	18 045	26	0.16
3	20 890	257	2.7
$(Ni^{II}(BEAAM))^-$			
1	16 900	48	0.33
2	21 640	294	3.0
$(Ni^{II}(emi))^{2-}$			
1	17 570	57	0.32
2	22 820	372	3.2

[a] All of these transitions were simulated using Gaussian line shapes. In addition to these transitions, a third or fourth transition at ~27 000–30 000 cm^{-1} was included to simulate the end absorbance. [b] $f = (4.61 \times 10^{-9})\epsilon\Delta_{1/2}$.

features we employed excited-state electronic structure calculations.

Electronic absorption spectra were simulated using the spectroscopy oriented configurational interaction (SORCI) approach (Figure 7 and Table 8), which is a multiconfigurational ab initio method.[24] This procedure divides the first-order interacting space into weakly and strongly perturbing configurations. The strongly perturbing configurations are treated variationally, while the weakly perturbing configurations are treated using second-order Møller–Plesset perturbation theory. Using the CAS(8,5) active space, we calculated the first four spin-allowed excitations for (bmmp-dmed)Ni^{II}, $(Ni^{II}(BEAAM))^-$, and $(Ni^{II}(emi))^{2-}$. This produced approximately 3.0×10^6 configurations per complex, of which ~2.5% were selected for. Although these spectra could be calculated with reasonable accuracy using TD-DFT methods, the SORCI procedure yielded a more accurate prediction of the transition oscillator strengths and excitation energies than the TD-DFT methods did (Supporting Information). An important difference between the SORCI and TD-DFT methods is that both the trends in excitation energy and oscillator strength across the series are reproduced in the SORCI calculations, while only the trends in the oscillator strengths are reproduced in the TD-DFT calculations.

In agreement with the hybrid-DFT calculations, the SORCI calculations found that the ground-state wave functions are derived mostly from the $\cdots(Ni(3d(\pi))/(S(\pi)^*))^2(Ni(3d_{x^2-y^2}))^0$ configuration.[34,35] The leading configuration ranges from 94.6% $\cdots(Ni(3d(\pi))/(S(\pi)^*))^2(Ni(3d_{x^2-y^2}))^0$ in the ground-state wave function for $(Ni^{II}(BEAAM))^-$ to 89.8% $\cdots(Ni(3d(\pi))/(S(\pi)^*))^2(Ni(3d_{x^2-y^2}))^0$ in the ground-state wave function for (dmmp-bmed)Ni^{II}. The other configurations that are significant contributors to the ground-state wave functions for these complexes are $\cdots(Ni/S/N(\pi))^0(Ni(3d_{z^2}))^2(Ni(3d(\pi))/S(\pi))^2(Ni(3d(\pi))/(S(\pi)^*))^2(Ni(3d_{x^2-y^2}))^2$, $\cdots(Ni(3d_{z^2}))^0(Ni(3d(\pi))/S(\pi))^2(Ni(3d(\pi))/(S(\pi)^*))^2(Ni(3d_{x^2-y^2}))^2$, $\cdots(Ni(3d(\pi))/(S(\pi)))^0(Ni(3d(\pi))/(S(\pi)^*)))^2(Ni-$

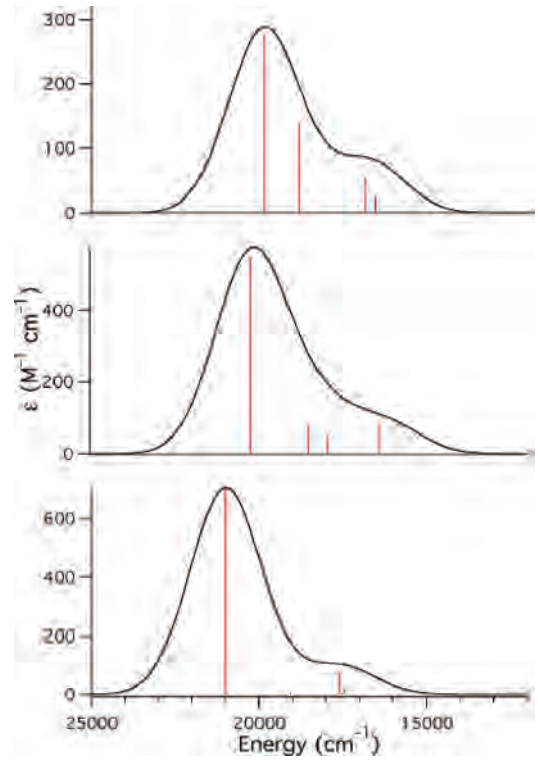

Figure 7. Calculated electronic absorption spectra highlighting the low-energy spin-allowed transitions for (bmmp-dmed)Ni^{II} (A), $(Ni^{II}(BEAAM))^-$ (B), and $(Ni^{II}(emi))^{2-}$ (C). Individual transitions are presented as red sticks and the spectra are simulated as Gaussian line shapes.

Table 8. Results from the SORCI Calculations for (bmmp-dmed)Ni^{II}, $(Ni^{II}(BEAAM))^-$, and $(Ni^{II}(emi))^{2-}$ Highlighting the Four Lowest-Energy Spin-Allowed Transitions

transition[a]	energy (cm^{-1})	f ($\times 10^{-3}$)
(bmmp-dmed)Ni^{II}		
85 → 86	16 526	0.18
84 → 86	16 822	0.39
83 → 86	18 800	0.10
82 → 86	19 855	1.9
$(Ni^{II}(BEAAM))^-$		
84 → 85	16 421	0.57
83 → 85	17 966	0.36
82 → 85	18 531	0.06
81 → 85	20 250	3.8
$(Ni^{II}(emi))^{2-}$		
83 → 84	17 455	0.15
82 → 84	17 602	0.52
81 → 84	19 072	0.05
80 → 84	20 992	4.9

[a] Indicates the leading configurations to the transition.

(34) The $\cdots$ indicates all orbitals below the specified orbitals are doubly occupied.

(35) The Ni(π) fragment is a linear combination of the 3d orbitals and is mostly composed of Ni($3d_{yz}$) and Ni($3d_{xz}$) nickel AOs.

$(3d_{x^2-y^2})^2$, and $\cdots(Ni(3d(\pi))/(S(\pi)^*)))^0(Ni(3d_{x^2-y^2}))^2$. The latter two configurations comprise ~2–3% of the ground-state wave functions each.

As might be predicted from the hybrid-DFT calculations, the first four spin-allowed excitations in all three complexes can be correlated to the HOMO → LUMO, HOMO−1 → LUMO, HOMO−2 → LUMO, and HOMO−3 → LUMO transitions. The use of these four excitations accurately reproduced the low-energy peak and shoulder in electronic absorption spectra of the three complexes investigated. From the SORCI calculations, we note two interesting trends in the two higher-energy excitations considered. We find that as one goes from $(Ni^{II}(emi))^{2-}$ to $(Ni^{II}(BEAAM))^-$ to (bmmp-dmed)Ni^{II}, the oscillator strength of the HOMO−2 → LUMO transition steadily increases. In contrast, the HOMO−3 → LUMO oscillator strengths follow the opposite trend: these decrease upon going from $(Ni^{II}(emi))^{2-}$ to $(Ni^{II}(BEAAM))^-$ to (bmmp-dmed)Ni^{II}. We can rationalize this by examining the configurations of the final-state wave functions in the HOMO−2 → LUMO and HOMO−3 → LUMO transitions.

For $(Ni^{II}(emi))^{2-}$ and $(Ni^{II}(BEAAM))^-$, the final state wave functions for the HOMO−2 → LUMO transitions are almost exclusively $\cdots(Ni/S/N(\pi))^2(Ni(3d_{z^2}))^1(Ni(3d(\pi))/S(\pi))^2(Ni(3d(\pi))/(S(\pi)^*))^2(Ni(3d_{x^2-y^2}))^1$ in character for both $(Ni^{II}(emi))^{2-}$ and $(Ni^{II}(BEAAM))^-$ (the wave functions are composed of >95% this configuration), while for (dmmp-bmed)Ni^{II}, there is significantly more mixing of the final-state wave function (the leading configuration is composed of 87.4% $\cdots(Ni/S/N(\pi))^2(Ni(3d_{z^2}))^1(Ni(3d(\pi))/S(\pi))^2(Ni(3d(\pi))/(S(\pi)^*))^2(Ni(3d_{x^2-y^2}))^1$). The final state for the HOMO−3 → LUMO transition in (dmmp-bmed)Ni^{II} contains 91.2% of the $\cdots(Ni/S/N(\pi))^1(Ni(3d_{z^2})^2(Ni(3d(\pi))/S(\pi))^2(Ni(3d(\pi))/(S(\pi)^*))^2(Ni(3d_{x^2-y^2}))^1$ configurations with very little contributions (<1%) from other configurations. This can be contrasted with $(Ni^{II}(emi))^{2-}$ and $(Ni^{II}(BEAAM))^-$ where the leading $\cdots(Ni/S/N(\pi))^1(Ni(3d_{z^2})^2(Ni(3d(\pi))/S(\pi))^2(Ni(3d(\pi))/(S(\pi)^*))^2(Ni(3d_{x^2-y^2}))^1$ configuration comprises 79.8% of the final-state wave function for $(Ni^{II}(emi))^{2-}$ and 75.6% of the final state wave function for $(Ni^{II}(BEAAM))^-$. Therefore the "allowedness" of the HOMO−2 → LUMO transition is increased in (dmmp-bmed)Ni^{II} relative to $(Ni^{II}(emi))^{2-}$ and $(Ni^{II}(BEAAM))^-$, and conversely, the allowedness of the HOMO−3 → LUMO transition is increased in $(Ni^{II}(emi))^{2-}$ and $(Ni^{II}(BEAAM))^-$ relative to (dmmp-bmed)Ni^{II} (i.e., there are several configurations in the ground- and final-state wave functions that make them nonorthogonal to one another).

The low-energy features observed in the experimental electronic absorption spectra were deconvoluted into 3−4 Gaussian peaks (Table 7).[36] The lowest-energy band occurs between 16 100 cm^{-1} for (bmmp-dmed)Ni^{II} and 17 70 cm^{-1} for $(Ni^{II}(emi))^{2-}$). Using the SORCI calculations as a guide, we can assign this band as being composed of the $S(\pi)/Ni(3d\pi)^* \rightarrow Ni(3d_{x^2-y^2})/S(\sigma)/N(\sigma)^*$ and the $S(\pi)/Ni(3d\pi) \rightarrow Ni(3d_{x^2-y^2})/S(\sigma)/N(\sigma)^*$ transitions (HOMO → LUMO and HOMO−1 → LUMO). In our experimental data, these two transitions are far too close together in energy to be meaningfully separated from one another in the spectral deconvolutions. For (bmmp-dmed)Ni^{II}, the $Ni(3d_{z^2}) \rightarrow Ni(3d_{x^2-y^2})/S(\sigma)/N(\sigma)^*$ transition (HOMO−2 → LUMO) occurs at ~1700 cm^{-1} higher in energy that the HOMO/HOMO−1 → LUMO transitions. Although this transition is contained in the low-energy shoulder of the experimental spectrum, it can be reproducibly extracted from the spectral data. In light of the SORCI calculations, we chose not attempt to separate this transition from the absorption data obtained for $(Ni^{II}(BEAAM))^-$ or $(Ni^{II}(emi))^{-2}$ because it would have too low of an intensity to be meaningfully deconvoluted from the data. The highest-energy transition that we extracted from the electronic absorption spectra is the $S(\sigma)/Ni \rightarrow Ni(3d_{x^2-y^2})/S(\sigma)/N(\sigma)^*$ transition (HOMO−3 → LUMO) and results in the well defined low-energy peak in these spectra. This transition occurs at 20 890 cm^{-1} for (bmmp-dmed)Ni^{II}, 21 650 cm^{-1} for $(Ni^{II}(BEAAM))^{2-}$, and 22 820 cm^{-1} for $(Ni(emi))^{2-}$.

Discussion and Biological Implications. In this study, Ni L-edge, S K-edge, and electronic absorption experiments, along with ab initio calculations, show that the Ni^{II} centers are highly covalent in all three $Ni^{II}N_2S_2$ complexes investigated. The S K-edge data shows that all three Ni-complexes have a high degree of S-character in the LUMO, ranging from 34(2)% S(3p) for (bmmp-dmed)Ni^{II} and $(Ni^{II}(BEAAM))^-$ to 27(2)% S(3p) for $(Ni^{II}(emi))^{2-}$. These results are in excellent agreement with our hybrid-DFT calculations performed on the three complexes.[33]

Both the high degree of covalency *and* the trend in Ni−S character is reflected in the corresponding force constants calculated for the Ni−thiolate bonds. We found that the Ni−S bonds in $(Ni^{II}(emi))^{2-}$ had the weakest calculated force constants of 1.39 mdyn $Å^{-1}$. In contrast the Ni−S bonds of (bmmp-dmed)Ni^{II} displayed calculated force constants of 1.51 and 1.50 mdyn $Å^{-1}$, corresponding to the shorter and longer Ni−S bonds, respectively. $(Ni^{II}(BEAAM))^-$ displayed calculated force constants that were intermediate between the two complexes, with the Ni−S bond trans to the amide N having a calculated force constant of 1.38 mdyn $Å^{-1}$ and the Ni−S bond *trans* to the amine nitrogen having a calculated force constant of 1.52 mdyn $Å^{-1}$. For comparison, these are stronger M−S force constants than those reported for several Fe^{III}−S proteins (1.20–1.36 mdyn $Å^{-1}$)[37] but weaker than those calculated for the highly covalent Cu^{II}−S bond of blue copper proteins (~1.9 mdyn $Å^{-1}$)[38] and oxidized NiSOD itself (1.79 mdyn $Å^{-1}$).[8b]

The conclusions reached from the S K-edge and electronic absorption studies are also consistent with our findings from the Ni L-edge studies. The Ni L-edge data demonstrate the progressive increase in ligand-field strength as the neutral amines were systematically replaced with anionic amide

(36) Two or three Gaussian peaks are used to simulate the transitions and one is used to simulate the end absorbance. The third or fourth peak is not reported.

(37) (a) Xiao, Y. M.; Wang, H. X.; George, S. J.; Smith, M. C.; Adams, M. W. W.; Jenney, F. E.; Sturhahn, W.; Alp, E. E.; Zhao, J. O.; Yoda, Y.; Dey, A.; Solomon, E. I.; Cramer, S. P. *J. Am. Chem. Soc.* **2005**, *127*, 14596. (b) Han, S.; Czernuszewicz, R. S.; Kimura, T.; Adams, M. W. W.; Spiro, T. G. *J. Am. Chem. Soc.* **1989**, *111*, 3505.

(38) Qiu, D.; Dasgupta, S.; Kozlowski, P. M.; Goddard, W. A.; Spiro, T. G. *J. Am. Chem. Soc.* **1998**, *120*, 12791.

ligands. Furthermore, the VBCI model and integrated L-edge intensities demonstrated the high degree of covalency in all three complexes. From the VBIC model, we demonstrate that the Ni($3d_{x^2-y^2}$) LUMOs are all highly covalent in nature. Hybrid-DFT calculations and the S K-edge results indicate that most of this is the result of the covalent Ni−S bonds. However, as there is an increase in the number of amide donors to Ni-center, the degree of Ni−N covalency also increases. Upon replacing one of the amine ligands in (bmmp-dmed)Ni^{II} with an amide, forming $(Ni^{II}(BEAAM))^-$, the amount of N character in the LUMO increases, while the degree of S character remains virtually unchanged. This is the result of an increase in the amount of S character in the thiolate trans to the amine and an equivalent decrease in the amount of S character in the thiolate trans to the amide. Going to the bis-amide complex $(Ni^{II}(emi))^{2-}$ further increases the degree of N character in the Ni($3d_{x^2-y^2}$) LUMO. However, the total percentage of S character dramatically decreases. This is reflected in the trend in the calculated transfer integral T_{B1g}; there is a nonsystematic change in T_{B1g} with $(Ni^{II}(BEAAM))^-$ displaying the largest transfer integral, followed by $(Ni^{II}(emi))^{2-}$ and then (bmmp-dmed)Ni^{II}. Furthermore, the other transfer integrals calculated in the VBCI model suggest there is a high degree of Ni−S covalency to the other orbitals in the d-manifold of $(Ni^{II}(BEAAM))^-$. This is reflected in the percentage of charge-transfer character in the ground-state wave function. Of the three complexes investigated in this study $(Ni^{II}(BEAAM))^-$ displayed the smallest degree of $|Ni3d^8\rangle$ character in its ground-state wave function, showing it is the most covalent of the three Ni^{II} complexes probed. This is further supported by the integration Ni L-edge spectra, which also show that $(Ni^{II}(BEAAM))^-$ is the most covalent LUMO of the Ni complexes investigated.

All of these data point to $(Ni^{II}(BEAAM))^-$ possessing highly covalent Ni−thiolate bonds. By analogy, this implies that the Ni^{II}−S bond in the NiSOD active-site is also highly covalent, as has been previously demonstrated using both the metalloenzyme and Ni^{II} and Ni^{III} model compounds.[6b,c,8,9] This high degree of covalency does not, however, imply that $(Ni^{II}(BEAAM))^-$ has the highest degree of S-character in its redox-active molecular orbital (RAMO; the HOMO). Compared with the other two $Ni^{II}N_2S_2$ compounds investigated in this study, we find that the RAMO of $(Ni^{II}(BEAAM))^-$ displays an intermediate degree of S-character when compared to bis-amine ligated (bmmp-dmed)Ni^{II} (which displays the highest degree of S character) and $(Ni^{II}(emi))^{2-}$ (which displays the lowest degree of S character). The trend in decreasing S character across the series is easily understood from the simplified MO diagram displayed in Scheme 2. Because of the decrease in the anionic charge of the ligand, the 3d AOs derived from Ni in (bmmp-dmed)Ni^{II} are significantly lower in energy than the S(π)/S(π)* fragments when compared to the other two complexes. In $(Ni^{II}(BEAAM))^-$, the Ni 3d AOs are destabilized relative to those in (bmmp-dmed)Ni^{II}, but still lower in energy than the S(π)/S(π)* fragments. As a result, the HOMO of $(Ni^{II}(BEAAM))^-$ is more covalent than that of (bmmp-dmed)Ni^{II} because of a better energy match between the Ni 3d AOs and the S(π)/S(π)* fragments. This creates an antibonding combination that still has a reasonably high degree of S content, but less S character than in (bmmp-dmed)Ni^{II}. In $(Ni^{II}(emi))^{2-}$, the Ni 3d AOs are even more destabilized relative to (bmmp-dmed)Ni^{II}, such that the Ni 3d AOs are now higher in energy than the corresponding S(π)/S(π)* fragments, which creates an antibonding combination that is predominantly Ni in character.

The consequences of these bonding interactions lead to dramatically different $1e^-$ oxidation behavior in (bmmp-dmed)Ni^{II} versus $(Ni^{II}(BEAAM))^-$ and $(Ni^{II}(emi))^{2-}$. Both amine/amide ligated $(Ni^{II}(BEAAM))^-$ and $(Ni^{II}(emi))^{2-}$ have reversible $1e^-$ redox couples[6c,10b] while (bmmp-dmed)Ni^{II} has an irreversible $1e^-$ oxidation couple.[10a] The reason for this is that the large degree of S-character in the RAMO of (bmmp-dmed)Ni^{II} will produce a S-centered oxidation, leading to the decomposition of the metal complex. In contrast the lower degree of S-character in both $(Ni^{II}(BEAAM))^-$ and $(Ni^{II}(emi))^{2-}$ leads to a Ni-centered, and hence reversible oxidation. Similar conclusions concerning the influence of amide ligation in $Ni^{II}N_2S_2$ complexes on their $1e^-$ oxidation process have been reached by us and others.[6c,8a,9a] It has been speculated by Brunold that the reduction in S-character effected by amide ligation is the key electronic feature of the NiSOD active-site that provides the enzyme protection from oxidative decomposition.[8a] We note that such conclusions are based on ground-state calculations performed on four-coordinate Ni^{II} centers. These conclusions must therefore be treated with caution when applied to the NiSOD active-site, which may be five-coordinate under catalytic conditions[39] and could also undergo significant electronic relaxation upon oxidation/reduction.[40]

We agree that a reduction in S-character in the RAMO is probably an important factor in stabilizing the Ni-center upon multiple redox processes. However, if this were the only factor dictating the stability of the active-site, one might argue that a bis-amide-ligated Ni-center would increase the stability of NiSOD. Such a situation is not the case.[6b] Our results point to another aspect of increased amide ligation to the Ni-center. A consequence of the increased destabilization of the Ni 3d AOs as the amine ligands are replaced with anionic amides is an increased covalency in the HOMO across the series upon going from (bmmp-dmed)Ni^{II} to $(Ni^{II}(emi))^{2-}$. Because the 3d manifold is shifted to higher energy, there is an increase in overlap between the Ni 3d AOs and the S(π)/S(π)* fragments (Scheme 2). This is observed in both the hybrid-DFT and SORCI calculations. Although the HOMO of $(Ni^{II}(emi))^{2-}$ has a higher degree of Ni than S character, the percentage of Ni and S AO character are more evenly balanced in these orbitals than in either $(Ni^{II}(BEAAM))^-$ or (bmmp-dmed)Ni^{II}. This indicates

(39) Neupane, K. P.; Gearty, K.; Francis, A.; Shearer, J. *J. Am. Chem. Soc.* **2007**, *129*, 14605–14618.
(40) (a) Kennepohl, P.; Solomon, E. I. *Inorg. Chem.* **2003**, *42*, 679–688. (b) Dey, A.; Glaser, T.; Couture, M. M.-J.; Eltis, L. D.; Holm, R. H.; Hedman, B.; Hodgson, K. O.; Solomon, E. I. J. *Am. Chem. Soc.* **2004**, *126*, 8320–8328.

that $(Ni^{II}(emi))^{2-}$ has the most covalent HOMO. This is followed by $(Ni^{II}(BEAAM))^{-}$ and then (bmmp-dmed)Ni^{II}. The practical consequence of this is that $(Ni^{II}(emi))^{2-}$ will have the highest-energy HOMO, followed by $(Ni^{II}(BEAAM))^{-}$ and then (bmmp-dmed)Ni^{II}.

In square-planar $Ni^{II}N_2S_2$ complexes, the Ni(3d(π))/S(π)* orbital is nucleophilic, and can reacts with O_2 and H_2O_2 forming a coordinated Ni-sulfenate.[3,10b] This trend in reactivity is readily observed in this series. In air-exposed MeCN solutions, both (bmmp-dmed)Ni^{II} and $(Ni^{II}(BEAAM))^{-}$ are stable with respect to oxidation while $(Ni^{II}(emi))^{2-}$ becomes oxygenated at sulfur within a minute.[6c] A S K-edge spectrum of the resulting oxidation product shows that one of the thiolates has been oxidized to a Ni-bound sulfenate, while the other remains a Ni-bound thiolate (Supporting Information).[12]

This observation aids in explaining the stability of the Ni-ligated cysteinates in NiSOD. By utilization of the mixed amide/amine ligand environment the HOMO is fine-tuned such that it does not react with O_2 forming a Ni-ligated sulfenate, as is formed at the Co and Fe centers of the bis-amide-ligated $M^{III}N_3S_2$ metalloenzyme nitrile hydratase for example.[4] This increased stability will undoubtedly increase the robustness of the Ni−S moiety toward $O_2^{\bullet-}$ and H_2O_2 as well. Alternatively, as has been pointed out by Darensbourg, Grapperhaus, and co-workers, the rate of catalysis in NiSOD ($k_{cat} > 10^9\ M^{-1}\ s^{-1}$) is significantly faster than the rate of sulfur based oxygenation by dioxygen.[9b] Therefore there is the possibility that the reason the Ni−S moiety remains unmodified in NiSOD is that it is kinetically stabilized as well; the oxygen-containing reactants and products found at the NiSOD active-site simply may not linger about the Ni-center long enough to promote sulfur-based oxygenation.

In all, this work shows that the coordinated nitrogen-based ligands at the active site of NiSOD are involved in finely tuning the electronic structure of the Ni^{II} ion. The combination of neutral amine and anionic amide ligands promotes Ni-centered one-electron oxidations while also deactivating the HOMO toward nucleophilic attack by dioxygen. Therefore, the unusual nitrogen based ligands found at the NiSOD active site are important in protecting the S-based ligands from oxidative damage.

Acknowledgment. The University of Nevada, Reno, is acknowledged for financial support of this work. X-ray absorption spectroscopy was performed at the National Synchrotron Light Source (Brookhaven National Laboratories) was supported by the U.S. Department of Energy, Office of Basic Energy Sciences, under Contact DE-AC02-98CH10886.

Supporting Information Available: Contains the normalized Ni L-edge spectra for (bmmp-dmed)Ni^{II}, $(Ni^{II}(BEAAM))^{-}$, and $(Ni^{II}(emi))^{2-}$, Ni L-edge spectra for (bmmp-dmed)Ni^{II}, $(Ni^{II}(BEAAM))^{-}$, $(Ni^{II}(emi))^{2-}$, and NiF_2, the S K-edge X-ray absorption spectrum of air-oxidized $(Ni^{II}(emi))^{2-}$, the B3LYP results for (bmmp-dmed)Ni^{II}, $(Ni^{II}(BEAAM))^{-}$, and $(Ni^{II}(emi))^{2-}$ using the crystallographic coordinates, and the results from the TD-DFT calculations for (bmmp-dmed)Ni^{II}, $(Ni^{II}(BEAAM))^{-}$, and $(Ni^{II}(emi))^{2-}$. This material is available free of charge via the Internet at http://pubs.acs.org.

IC7019878